

See discussions, stats, and author profiles for this publication at: <https://www.researchgate.net/publication/273464954>

Reactive and Inelastic Channels in the $\text{Ca}^* \cdots \text{FCH}_3$ Transition State: A Simple Branching Mechanism

ARTICLE in THE JOURNAL OF PHYSICAL CHEMISTRY A · MARCH 2015

Impact Factor: 2.69 · DOI: 10.1021/acs.jpca.5b00444 · Source: PubMed

READS

18

8 AUTHORS, INCLUDING:



Eric Gloaguen

French National Centre for Scientific Research

64 PUBLICATIONS 424 CITATIONS

SEE PROFILE



Steven Stolte

Jilin University

236 PUBLICATIONS 4,125 CITATIONS

SEE PROFILE



Lionel Poisson

French National Centre for Scientific Research

106 PUBLICATIONS 929 CITATIONS

SEE PROFILE



B. Soep

Atomic Energy and Alternative Energies Com...

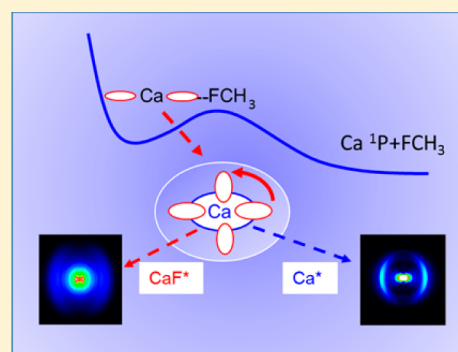
155 PUBLICATIONS 2,253 CITATIONS

SEE PROFILE

Reactive and Inelastic Channels in the $\text{Ca}^*\cdots\text{FCH}_3$ Transition State: A Simple Branching MechanismM. Briant,^{†,‡} E. Gloaguen,^{†,‡} A. Beswick,[§] J. M. Mestdagh,^{†,‡} S. Stolte,^{†,‡,||,⊥} L. Poisson,^{†,‡} C. Pothier,^{†,‡} and B. Soep^{*,†,‡}[†]Laboratoire Francis Perrin, LIDyL, DSM IRAMIS, CEA Saclay, and [‡]Laboratoire Francis Perrin, CNRS URA 2453 CEA, Saclay, F-91191 Gif Sur Yvette, France[§]LCAR IRSAMC, Université de Toulouse 3, F-31062 Toulouse, France^{||}Institute of Atomic and Molecular Physics, Jilin University, Changchun, 1300012, China[⊥]Department of Physics and Astronomy, LaserLaB, Vrije Universiteit, De Boelelaan 1081, 1081 HV Amsterdam, The Netherlands

S Supporting Information

ABSTRACT: To study the excited state dynamics between a calcium atom and the CH_3F molecule, a $\text{Ca}\cdots\text{CH}_3\text{F}$ 1:1 complex has been prepared by a supersonic expansion with laser ablation of calcium metal in the gas phase. Tunable laser excitation of these complexes in molecular states correlating to $\text{Ca } ^1\text{P}_1(4s4p) + \text{CH}_3\text{F}$ allows observing two competitive channels: the direct dissociation and the reactive channel into $\text{CaF}^* + \text{CH}_3$. The translational recoil, as well as the alignment of the fragments Ca^* and CaF^* have been analyzed by velocity map imaging and time-of-flight mass spectrometry. This revealed that both the dissociation and reaction processes are quasi direct and are of comparable intensity. We provide a simple interpretation for this process: the electronically excited potential surface of the $\text{Ca}^*\cdots\text{FCH}_3$ complex initiates a fast predissociation from a suspended well to two repulsive surfaces that lead either to $\text{Ca } ^1\text{P}_1(4s4p)$ ($\Omega = 1$) + CH_3F or to $\text{CaF}(^2\Delta) + \text{CH}_3$.

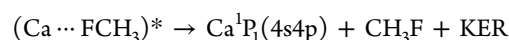


I. INTRODUCTION

The direct excitation of the transition state range of an excited state bimolecular reaction provides a powerful means to explore the potential energy surface (PES) in this key region for free^{1–5} or deposited systems.⁶ This approach has focused so far on the spectroscopic aspects in the molecular frame of the cluster, i.e., of the reactive system, on the possibility to detect time evolution⁷ and on the energy partition between the internal degrees of freedom (electronic, vibrational and rotational).⁸ The determination of the kinetic energy release (KER) has been largely indirect in these experiments, in contrast with the corresponding photodissociation experiments. Nevertheless, observing the KER is essential because it informs directly on the energy surface beyond the transition region, in a region of the PES not accessible to direct optical excitation of a reacting complex. Here, we report on such experiments, where the KER is measured after photoexcitation of a bimolecular complex. $\text{Ca}\cdots\text{FCH}_3$ has been chosen as an example because it appears as a model system for transition state spectroscopy for the reaction of excited metal atoms with polyatomic molecules. We have adopted here a different approach from previous studies:^{9–11} the determination of the KER of the fragments and their alignment with the exciting laser polarization. This probes the transition state from the fragments side. We have investigated two open, competing, channels in the 3.18–3.35

eV energy region above the $\text{Ca } (4s4p) ^1\text{P}_1$ atomic state. These channels are the direct dissociation:

Channel 1



and the excited state reaction as in refs 9–11

Channel 2



The observation of the KER on each channel has allowed a precise description of the mechanism leading to the separation between the two channels. A similar situation had been observed in the dynamics of another electronically excited molecular complex ($\text{Ba}\cdots\text{FCH}_3$) A' but analyzed by time dependent methods.¹² However, in this case, the A' state connects only to channel 1, through a repulsive surface. We show here that the competition between channel 1 and channel 2 arises from a specific potential energy surface with a suspended well that predissociates into two competing channels. The experimental results have been complemented

Special Issue: Jean-Michel Mestdagh Festschrift

Received: January 15, 2015

Revised: March 10, 2015

Published: March 12, 2015



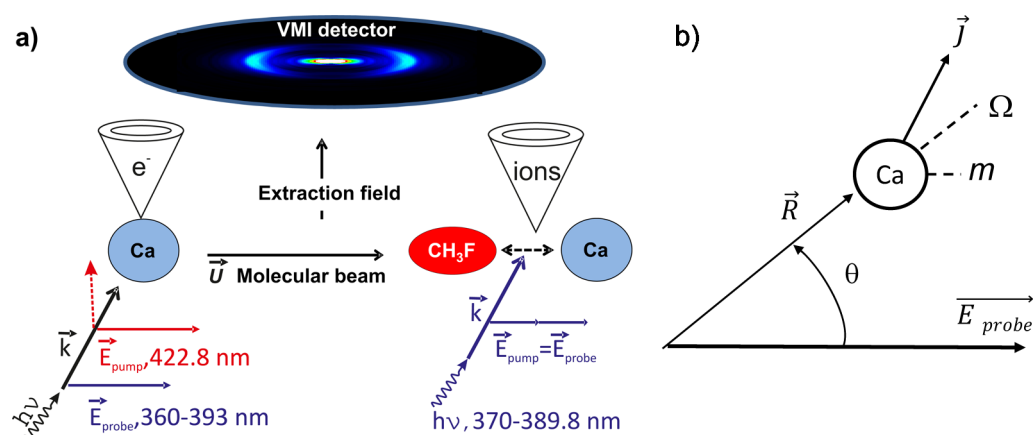


Figure 1. (a) Arrangement of the VMI setup used for electrons or ions, free atoms or atoms resulting from photodissociation. The polarization vector \vec{E}_{probe} of the probe laser beam is parallel to the molecular beam and to the plane of the VMI detector. In the study of the free Ca atom, the polarization vector of the pump beam, \vec{E}_{pump} can be in either parallel or perpendicular configurations. (b) Vector diagram of the momenta in the recoil frame: the electronic angular momentum \vec{j} is projected as Ω along \vec{R} whereas in the lab frame as m on \vec{E}_{probe} . The molecular frame $|j\Omega\rangle$ states prepared through the dissociation are projected in the lab (probe laser) frame as $|jm\rangle$.

by quantum chemistry calculations to document the dissociation channel toward $\text{Ca} + \text{CH}_3\text{F}$. Potential energy surfaces correlating up to $\text{Ca}^1\text{S} (4s5s) + \text{CH}_3\text{F}$ have been considered.

II. EXPERIMENTAL SECTION

The present setup allows measurement of the fragment recoil from photoexcited $\text{Ca}\cdots\text{FCH}_3$ van der Waals complexes created from a laser ablation source. The general setup has been described in previous publications;^{9,10} however, there, the goal was to obtain spectra, not recoil energy distributions. Therefore, two additional methods have been implemented: the analysis of mass profiles from time-of-flight mass detection and ion velocity map imaging.¹³

Briefly, complexes are formed in the expansion of an helium–methyl fluoride mixture (<5%) by a piezoelectric valve in the Trickl design.¹⁴ A calcium rod is rotated tangentially to the gas channel and a focused frequency doubled Nd:YAG laser (0.5 mJ) ablates the surface of the metal. Accurate timing is required so that firing of the laser occurs in the early maximum of the gas pulse. The system is operated at a total backing pressure in the 2.5–3.5 bars range. In these conditions, the concentration of the complex amounts to $\sim 1\%$ of the calcium present in the beam. The concentration of $\text{Ca}\cdots(\text{FCH}_3)_2$ was maintained lower than 10% of the corresponding $\text{Ca}\cdots(\text{FCH}_3)$ complex as described in ref 9. During the expansion calcium metastables (^1D , ^3P , ^3D) resulting from the ablation will collide and react with CH_3F seeded in the helium expansion, forming CaF and eventually metastable $\text{CaF B}'(^2\Delta)$.

After skimming, in the second chamber pumped by a cryopump (Coolstar 3500 L/s Edwards), the cluster beam is directed into a Wiley–McLaren¹⁵ time-of-flight mass spectrometer with a 1 m path collinear with the beam (TOF). Alternatively, it is passed through a velocity map imaging device (VMI ion or electron), operated perpendicular to the molecular beam with the Eppink–Parker design.¹³ The recoil of the dissociating and reacting $\text{Ca}\cdots\text{FCH}_3$ system has been recorded in two ways by monitoring (i) in the VMI, the velocity distribution relative to the laser polarization parallel to the detector and to the molecular beam, Figure 1a, and (ii) in a second type of experiments, the velocity recoil in the acceleration region of the TOF. In this latter experiment, if the recoil velocity is parallel to the molecular beam axis, the

calcium atom or CaF will move in two directions toward the detector or away from it, splitting the mass peaks by different time appearances on the detector. This approach follows the photodissociation studies of the $\vec{\mu}$, \vec{v} (transition dipole, recoil velocity) correlations by fluorescence¹⁶ or mass spectrometry¹⁷ detection.

Although VMI is the ultimate technique, providing detailed information on the alignment of the recoiling fragments, recoil within a TOF is simple and allows a quantitative direct comparison of the recoiling channels because all fragments are observed simultaneously.

The velocity distributions and alignments are derived by image inversion of the raw VMI images using the pBasex algorithm.¹⁸ The analysis yields an expansion of the radial velocity distribution in even-order Legendre polynomials, where $I(\theta)$ is the total radial averaged angular dependence of the distribution (θ_e for electrons or θ for ions) and $P_0 = 1$:

$$I(\theta) = I \cdot [1 + \beta_2 \cdot P_2(\cos \theta) + \beta_4 \cdot P_4(\cos \theta) + \beta_6 \cdot P_6(\cos \theta) + \dots] \quad (1)$$

The mass profiles in the TOF are simulated by forward convolution using an a priori velocity distribution of the fragments, McLaren's equations,¹⁵ and the apparatus function derived from a recoil-free profile (Supporting Information). The mass profiles are recorded for the parallel and perpendicular orientations of the laser polarization with respect to the beam velocity (same laser for the pump and the probe).

III. THEORETICAL DETAILS

The quantum chemistry calculations have been performed in the same spirit as those of refs 9, 10, and 19 using the MOLPRO *ab initio* package.²⁰ The core electrons of calcium have been described by a $[\text{Ca}^{2+}]$ effective potential, complemented by a core-polarization potential (see ref 19 for details). An uncontracted $[9s,8p,7d]$ valence Gaussian basis set has been used to describe calcium. All the electrons of the C, F, and H atoms in CH_3F have been considered and the aug-cc-pVDZ basis set has been used for their description.²¹ The electronic problem was solved under the C_s geometry at the MRCI (multiconfiguration reference internally contracted configuration interaction^{22,23}) level of calculation. The

reference states have been derived using the general MCSCF/CASSCF program called MULTI of the MOLPRO package.^{24,25} In this calculation, the 1s electrons of C and F are kept frozen and the other electrons of CH₃F are in closed shells (5A', 2A''). The active space corresponds to 2 electrons in 28 active orbitals (17A' and 11A''). The MULTI calculation is state averaged over 7 ¹A', 3 ¹A'', 6 ³A', and 3 ³A'' states. At large separation between Ca and CH₃F, this corresponds to electronic excitation of singlet and triplet states up to the 4s5s ¹S and 4s5s ³S states. The same active space has been used in the MRCI calculation, keeping the core and closed orbitals of the MULTI calculation as core orbitals. As in the MULTI calculation, 7 ¹A', 3 ¹A'', 6 ³A', and 3 ³A'' states have been considered in the MRCI calculation.

With these choices, a reliable prediction of the calcium energy levels has been obtained at large separation between calcium and CH₃F. The results are shown in Table 1.

Table 1. Comparison between Calculated Calcium Energy Levels (Present Work) and Experiment

energy levels	calculated (cm ⁻¹)	experiment (cm ⁻¹) ²⁶	exp - calc (cm ⁻¹)
4s ² ¹ S	0	0	0
4s4p ³ P	15041	15263.089	-222
4s3d ³ D	20313	20356.625	-44
4s3d ¹ D	21788	21849.634	-61
4s4p ¹ P	23119	23652.304	-534
4s5s ³ S	31207	31539.495	-333
4s5s ¹ S	33125	33317.264	-192

When the CH₃F molecule is at a finite distance from Ca, the Ca position with respect to CH₃F is given by the Ca–F distance (R_{CaF}) and the Ca–F–C angle (A_{CaFC}). The azimuthal position of Ca is chosen for a planar symmetry of the Ca...FCH₃ complex. The R_{CaF} distance has been sampled in 28 steps between 1.95 and 10 a_0 , and the A_{CaFC} angle, between 0 and 180° by 10° steps. At each point that samples the Ca position,

the coordinates describing the CH₃F moiety of the complex has been optimized at the RHF level prior the MULTI and MRCI calculations.

IV. RESULTS

The experiments have been performed in two steps, first observing the ionization properties of the free calcium atom present in the molecular beam together with the Ca...FCH₃ complex, by photoelectron spectroscopy in the VMI setup. Second, with this information we could quantify the recoil velocity and velocity alignment of the electronically excited calcium atom produced from the dissociation of the electronically excited complex.

IV.A. Stepwise Ionization of Free Ground State Atomic Calcium via Its ¹P₁(4s4p) Electronically Excited State.

To determine the angle dependent ionization properties of Ca ¹P in the 360–393 nm domain, velocity map imaging of electrons has been used to detect free ground state ¹S(4s²) calcium atoms provided by the supersonic expansion under expansion conditions where complexes are not formed. Free Ca ¹S(4s²) has been ionized in a 1 + 1', two-photon sequential excitation scheme via resonant excitation of the ¹P(4s4p) ← ¹S(4s²) transition at 422.8 nm (photon 1), followed by ionization with a tunable laser (photon 1'). The corresponding results are shown in Figure 2. With the pump at 422.8 nm, the ionization laser has been tuned from the threshold at 390.3 nm for ionization of the ¹P state to 360 nm, encompassing the monitoring energy range for the complex (400–370 nm).

In Figure 2a,b, the polarization of the exciting laser beam 1 is parallel to the VMI detector plane and the ionization laser 1' is also parallel to it (Figure 1a). Laser 1 creates a p orbital, $m = 0$ aligned along its polarization. *A priori*, ionization of this orbital leads to a superposition of s and d electron waves in a ratio that is expected to depend upon the excess energy above the ionization potential. However, by determining the components $P_4(\theta_e)$ and $P_2(\theta_e)$ in the analysis of the images, we found an

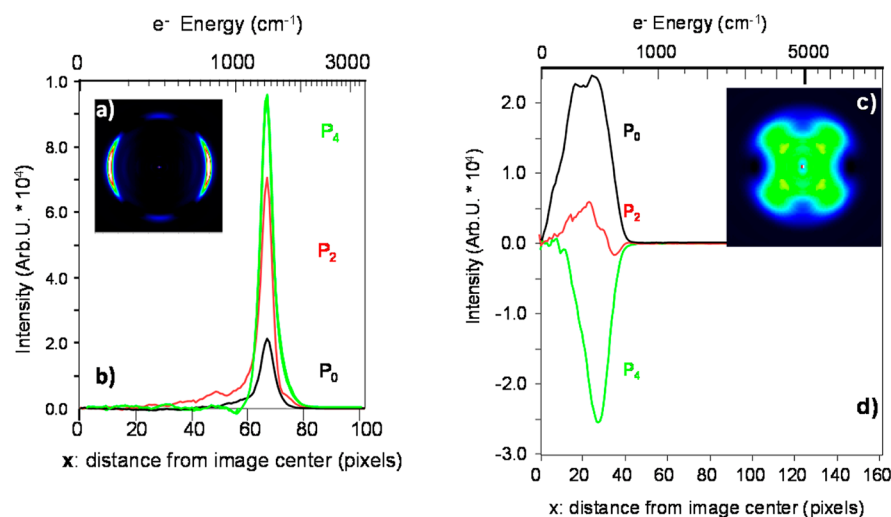


Figure 2. Photoelectron detection of free atomic calcium from the beam using the 1 + 1' resonant two-photon ionization scheme $\text{Ca } ^1\text{S} \rightarrow \text{Ca } ^1\text{P} \rightarrow \text{Ca}^+ ^2\text{S}$ described in the text. In the left part of the figure, the Ca (4p) orbital has been aligned parallel to the detector plane by the horizontal polarization of the 422.8 nm laser, hence preparing Ca ¹P(4s4p) $m = 0$. There, the 370 nm (1') ionization laser is parallel to both the detector plane and the pump laser. The inset (a) shows an inverted image of the electron distribution and under it, in (b), the even-order (P_0 , black; P_2 , red; P_4 , green) Legendre polynomial analysis of the image. On the right of the figure, the same settings, but the polarization vector of the 422.8 nm pump laser points perpendicular to the detector plane (Ca ¹P(4s4p) $m = 1$ is prepared) and the ionization laser at 387.5 nm has a polarization parallel to the detector.

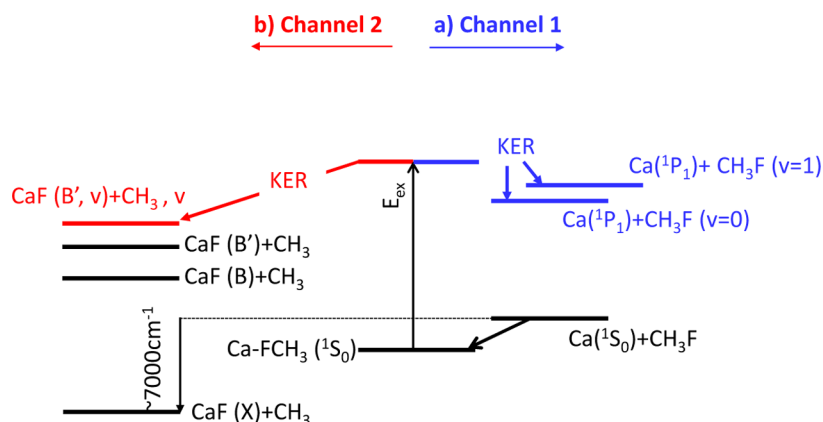


Figure 3. (Right) diagram of the energetics and KER of the dissociation eq 6 for channel 1 (blue). (Left) same for channel 2 (red).

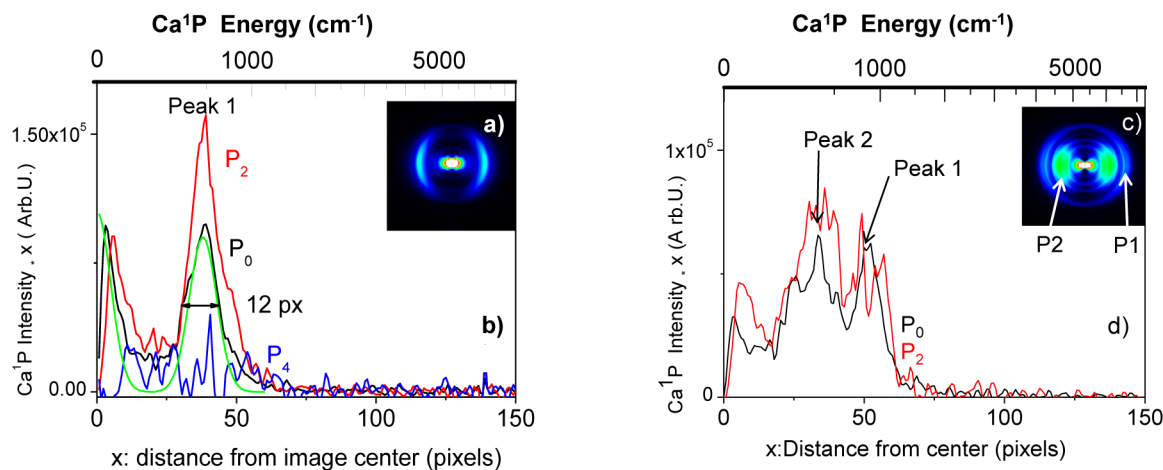


Figure 4. (a) Recoil of the Ca atom dissociated at 390 nm after transformation with the pBasex program. (b) Integrated radial distribution for the Legendre expansion in P_0 (black), $P_2(\theta)$ (red), and $P_4(\theta)$ (blue) polynomials. Represented in green, the Gaussian fit of the beam velocity spread with a 12 pixels full width half-maximum, FWHM (arrows). The horizontal scale is in image pixels, i.e., in velocity space (1 pixel = 13.8 m/s for Ca atoms), the vertical scale is arbitrary units \times . (c) Same as (a) but excitation at 376 nm. (d) Integrated radial distributions for the Legendre expansions in P_0 (black) and $P_2(\theta)$ (red) of image (c). P2 and P1 indicate the positions of peaks 1 and 2 on the transformed image (c).

almost constancy of the d/s waves over the range 387.5–360 nm, with a high value for the $P_4(\theta_e)$ component. As shown in the paragraphs below, this signals an important contribution of d waves, which overwhelms that of s waves.

Indeed, the angular distributions of the photoelectrons ejected from the ionization of atomic Ca $1P(4s4p)$ atoms allow a direct determination of the electron waves. If one assumes that the d electron wave is dominant, the angular distribution $I(\theta_e)$ of the electrons should match that of a $l = 2$, $m = 0$ wave function $(Y_0^2)^2$ of a d_z^2 wave, i.e.,

$$I(\theta_e) = I \cdot (3(\cos \theta_e)^2 - 1)^2 \quad (2)$$

which can be expanded in even-order Legendre polynomials as in eq 1:

$$I(\theta_e) = I \cdot [1 + (10/7) \cdot P_2(\theta_e) + (18/7) \cdot P_4(\theta_e)] \quad (3)$$

The predicted ratio of β_4/β_2 from (eq 3) is therefore 1.8, and the experimental value from Figure 2 is 1.35 ± 0.2 . Similarly, β_4 is 2.57 compared to $\sim 3.5 \pm 0.4$ for the experimental value. This must be considered as satisfactory because the expected order of intensities $P_4(\theta_e) > P_2(\theta_e) > 1$ is reproduced by the experiment.

In addition, the ionization in the $m = 1$ configuration has also been performed using the same polarization for the ionization

but a perpendicular polarized pump laser beam directed toward the VMI detector. The resulting inverted image is shown in Figure 2c, and the expansion of the angular distribution in radial averaged Legendre polynomials is shown in Figure 2d. It shows a small β_2 , but a high negative β_4 . In the same manner as in the preceding, one finds from a $(d_{xz})^2$ angular distribution of the electrons, the following expansion in Legendre polynomials:

$$I(\theta_e) = I \cdot [1 + (5/7) \cdot P_2(\theta_e) - 2 \cdot P_4(\theta_e)] \quad (4)$$

in fair agreement with Figure 2d.

Experimentally, the change in angular distribution between the $m = 0$ (d_z^2) and $m = 1$ (d_{xz}), is the indication for the nature of the electron wave, confirmed by the adequate ratios of the Legendre polynomials in the (d_z^2) wave. We therefore consider that the ionization of Ca ($1P$) with $\lambda < 380$ nm as yielding essentially pure d electron waves.

IV.B. Observation of the Ca $1P(4s4p)$ Recoil in Channel 1 (Photodissociation). The two complementary methods, velocity map imaging of the recoiling excited calcium fragment and time-of-flight recoil mass profiles, have been used to measure the recoil velocity distribution and alignment with respect to the direction of polarization of the photodissociation laser. In both cases, the recoiling Ca $1P(4s4p)$ atoms are probed by photoionization and photoions are detected. Note that in

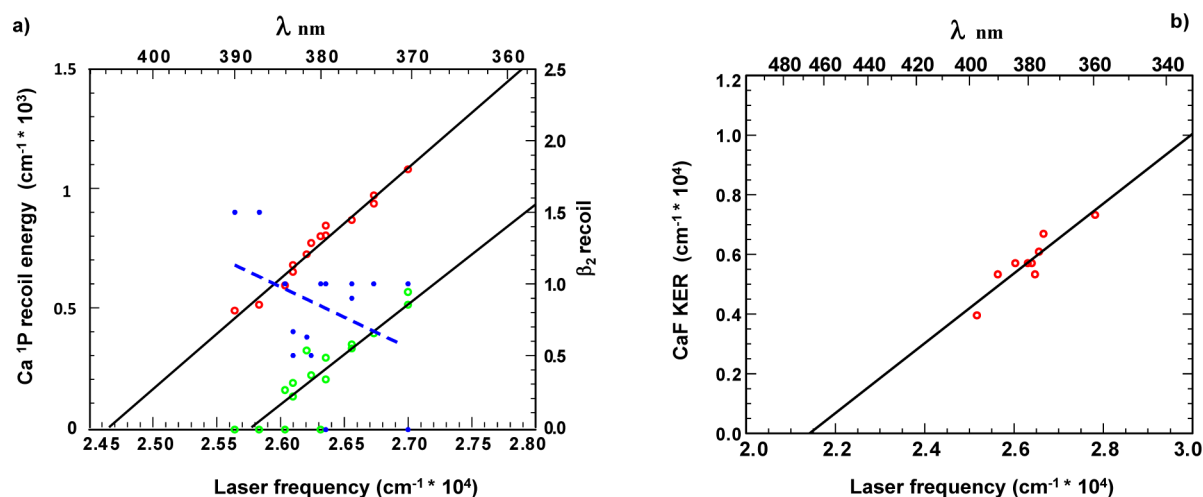


Figure 5. (a) Plot of the two recoil energy peaks (peak 1 = red open circles, peak 2 = green) of the $^1\text{P}(4s4p)$ calcium atom versus laser frequency, extrapolating respectively at 24 657 (405.56 nm) and 25 774 cm⁻¹ (387.99 nm). Note that the energy plotted is the measured recoil energy of Ca, not the KER. The anisotropy β_2 is also shown for peak 1 in blue solid circles and a blue dashed line between the points. (b) Plot of the total KER energy corresponding to the peak in the P_2 component of the velocity distribution of CaF (red open circles), as a function of the laser frequency in wavenumbers. The extrapolated value to zero recoil is 21 420 cm⁻¹.

contrast, photoelectron detection is not possible because of the simultaneous presence with Ca*, of CaF* (channel 2), whose broad electron distribution upon ionization would smear out the Ca $^1\text{P}(4s4p)$ electron distribution (Figure 3).

a. VMI Observation of Channel 1, Monitoring Ca⁺ Ions.

On Ca...FCH₃, the ion imaging process operates by a 1 + 1 scheme: the first photon excites Ca...FCH₃ electronically in the 360–390 nm region, causing dissociation via channel 1, during the laser pulse (5 ns). The resulting Ca $^1\text{P}_1(4s4p)$ atom then absorbs a second photon from the same laser pulse and ionizes. VMI measurements are performed starting from the ionization energy threshold of the resulting Ca $^1\text{P}_1(4s4p)$ atom with the second photon. Given the electric field in the ionization region, the threshold of the Ca⁺ $^2\text{S}_{1/2}(4s) \leftarrow \text{Ca } ^1\text{P}_1(4s4p)$ ionization, at 389.8 nm, is Stark shifted to 390.3 nm (Supporting Information S2). The observation of Ca $^1\text{P}_1(4s4p)$ can occur at this wavelength because the complex is already above the dissociation threshold after excitation by the first photon.

Panels b and d of Figure 4 represent the velocity distributions of ejected Ca($^1\text{P}_1$) as deduced from Figure 4a,c, through radial integration of the different contributions of the anisotropy with respect to the ionization laser: P_0 (isotropic contribution), $P_2(\theta)$, $P_4(\theta)$. It is observed in Figure 4b that the velocity distribution of recoiling Ca ^1P is narrow, 12 pixels (FWMH). It is broadened by the velocity spread in the molecular beam. The contribution of this translational broadening can be estimated as ~12 pixels, determined from the central spot. This spot pertains most probably to free calcium in the beam, nonresonantly ionized (note that the relative number density of the Ca atom and the complex is ~100/1). Therefore, the observed recoil distribution width of ejected calcium is essentially instrumental as the green simulation curve matches the P_0 experimental peak distribution.

Also, from Figure 4, one sees an important contribution of the second-order anisotropy, yielding $\beta_2 = 1.6 \pm 0.15$ following eq 1. On the contrary, the $P_4(\theta)$ contribution is weak $\beta_4 \approx 0.16 \pm 0.1$ in the recoil distribution of Figure 4a.

The variation of the recoil energy of Ca (^1P) with laser energy is plotted in Figure 5, using peaks 1 and 2 of Figure 4. The recoil energy nicely extrapolates linearly to zero at 24 660

cm⁻¹ (405.5 nm) for peak 1. This corresponds to the threshold for dissociation in the electronic state of the complex correlating with the Ca $^1\text{P}_1(4s4p)$ asymptote. Also, another peak is found in the velocity distribution with lesser recoil (peak 2 in Figure 4c,d), and the corresponding extrapolation of the green points as a function of laser frequency leads to a higher value ~25 800 cm⁻¹ (387.5 nm), Figure 5a. Peak 2 in the velocity distribution is very weak in the 370–390 nm absorption region and becomes as intense as peak 1 at 376 nm, Figure 4d.

From the $P_2(\theta)$ component in the polynomial analysis in Figure 4a, one obtains $\beta_2 = 1.6 \pm 0.15$ and $\beta_4 = 0.16 \pm 0.1$. The anisotropy of the recoil of the Ca atom from the complex is high. β_2 decreases slightly with excess energy and has an energy average value of 1. The atom in the molecular Ca...FCH₃ molecular frame is dissociated in a $\Omega = 0$ or 1 state, where Ω is the projection of the total electronic momentum j of Ca, along the Ca...FCH₃ axis (Figure 1b). However, the atom is detected in the laboratory frame and j is referenced to it via the laser polarization axis, as a function of the m laboratory states.

A Ca(^1P) atom, which is ejected in the direction θ with respect to the polarization of the dissociation laser, experiences an angle dependent ionization probability $W(\theta)$ because a Ca(Ω) state in the molecular frame is a θ dependent linear combination of Ca(m) states in the laboratory frame. The calculation gives (Appendix)

$$W(\theta) \propto 1 + (1/3) \cdot (\cos \theta)^2 \quad \text{for } \Omega = 0$$

$$W(\theta) \propto 1 - (1/7) \cdot (\cos \theta)^2 \quad \text{for } |\Omega| = 1$$

Because in the reaction (channel 1), the Ca atom is ejected with an angular distribution $(1 + \beta_{2\text{diss}} P_2(\theta))$, the resulting observed angular distribution of ionized Ca atoms will be given by

$$I(\theta) \propto W(\theta) \cdot (1 + \beta_{2\text{diss}} P_2(\theta)) \quad (5)$$

and leading for $\Omega = 1$ to (Appendix)

$$I(\theta) \propto [(70 - 7\beta_{2\text{diss}}/5) + P_2(\theta) \cdot (68\beta_{2\text{diss}} - 7) - (18/5) \cdot P_4(\theta) \cdot \beta_{2\text{diss}}] \quad (5b)$$

Therefore, the observed alignment β_2 of the recoiling Ca can be written, as in eq 1:

$$\beta_2 = (68 \cdot \beta_{2\text{diss}} - 7) / (70 - 7\beta_{2\text{diss}}/5) \quad \text{with} \quad (|\Omega| = 1) \quad (5c)$$

Equation 5b yields a high recoil anisotropy β_2 , together with a small β_4 , in agreement with the observations of Figure 4. The resulting recoil anisotropy $\beta_{2\text{diss}}$ is found, using eq 5c with $|\Omega| = 1$ in the range $1.1 \pm 0.1 \leq \beta_{2\text{diss}} \leq 1.7 \pm 0.15$ (as $1 \pm 0.1 < \beta_2 < 1.5 \pm 0.15$), depending on the laser wavelength (cf. Figure 4a).

b. TOF Observation of Channel 1, Monitoring the Recoil Velocity of $\text{Ca}^1\text{P}_1(4s4p)$. The recoil of calcium appears direct, as seen in Figure 4, with the Ca fragment aligned along the laser polarization axis. This generates two different profiles for the mass peaks in the observation by time-of-flight spectrometry, whether the polarization axis of the laser is parallel or perpendicular to the axis of the TOF spectrometer. In the parallel configuration of the dissociating polarization laser with the TOF axis, a distribution of velocities (radial and angular) is generated along this axis, with molecules flying against or along the acceleration direction in the TOF as shown in Supporting Information S1. This produces a typical “rabbit ear” shape for parallel type excitation. The simulations for parallel and perpendicular traces are shown in Figure 6 and have been

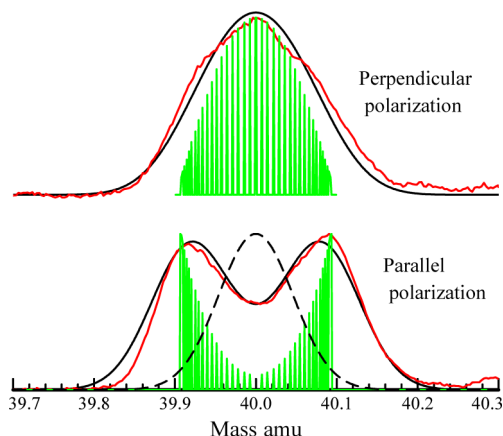


Figure 6. Mass peak of recoiling calcium has been observed in two configurations: top dissociation-ionization laser (390 nm) perpendicular to the beam/TOF axis, bottom parallel to the axis. In red is the experimental curve, and in black, the simulation. The simulation parameters are the same for the parallel and perpendicular case: the recoil KER distribution peaks at 500 cm^{-1} for the excited calcium atom, the β_2 dissociation anisotropy is adjusted at $\beta_{2\text{diss}} = 1.6$, and the angle dependent ionization probability is $(1 - (1/7) \cdot \cos^2(\theta))$. The green bars are the unconvoluted mass profiles with parallel or perpendicular excitation. The dashed curve is the apparatus function deduced from the free calcium profile and used to convolve the ejected mass profile.

made with the following parameters $\beta_2 = 1.5$ and a KER recoil energy of 500 cm^{-1} for the excited calcium atom, equivalent to the values deduced from Figure 4a. The velocities are projected along the beam axis from a preferentially parallel or perpendicular dissociation depending upon the electric vector respectively parallel or perpendicular to the beam. The projections are then convoluted with the mass profile for a

nonrecoiling element, i.e., the free Ca atom. The recoil for CaF has also been observed in the same conditions and exhibits also a highly and anisotropic velocity distribution.

IV.C. Recoil of the CaF Fragment Recoil, in Channel 2.

The recoil of CaF in channel 2 is easily observed by selecting mass 59.1 amu with the time gate in the VMI. It shows a significant recoil of 1200 cm^{-1} at 370.1 nm for CaF, indicating a significant excess energy as in Figure 7 left. This transforms into the total recoil energy in the center of mass of the two fragments CaF^{**} and CH_3^* . Using the mass ratio of the other fragment CH_3^* and the total mass of the complex (74.1 amu), the KER is obtained as $1200 \times 74.1/15 = 6000 \text{ cm}^{-1}$.

The total recoil energy is found to vary approximately linearly with excess energy as shown in Figure 5b, with a slope of 0.23. The coefficients of the two Legendre expansions $P_2(\theta)$ and P_0 exhibit different profiles with the fastest velocities showing the largest anisotropies; at pixel 70, for example, $\beta_2 \approx 1.6 \pm 0.15$, while at pixel 25, $\beta_2 \approx 0.4 \pm 0.1$. The double velocity distribution is also manifest in the mass profiles, as shown in Figure 7 right, where a central peak of unpolarized CaF appears in the parallel and perpendicular velocity configurations. The distribution centered close to zero kinetic energy results probably from background metastable $\text{CaF}(\Delta)$ state created at the tip of the ablation source by reaction of calcium metastables with CH_3F .

V. DISCUSSION

The excited state dynamics of the $\text{Ca} \cdots \text{FCH}_3$ complex are briefly presented as background for the discussion of the present results. It follows essentially from previous transition state spectroscopy experiments of the present group, complemented by *ab initio* calculations.^{9–11}

The Ca, FCH_3 system is $\approx 7000 \text{ cm}^{-1}$ above the reaction threshold in the ground electronic state from thermodynamics.^{27,28} However, it is trapped behind a barrier, which blocks the reaction. The geometry of the $\text{Ca} \cdots \text{FCH}_3$ system is slightly bent (the Ca–F–C angle = 170°) with calcium pointing toward the fluorine atom.¹⁰ The potential energy surface (PES) is only weakly anisotropic with a barrier to rotation of only 220 cm^{-1} , compared to the 850 cm^{-1} calculated binding energy. One can reach by Franck–Condon excitation a wealth of excited PES's that correlate with the electronic states of the excited calcium atom $^1\text{D}_2$ ($3d4s$) and $^1\text{P}_1$ ($4s4p$) and ^1S ($4s5s$) at large separation between Ca and CH_3F . The action spectra corresponding to excitation toward these surfaces have been observed by monitoring the CaF^* product by ionization and interpreted using quantum *ab initio* calculations. The reaction proceeds through the excited state harpoon mechanism and thus releases impulsively much energy in the electronic, vibrational, rotational, and translational degrees of freedom of the CaF product. However, calculations have shown the existence of large barriers (up to 1 eV in Figure 8 of ref 9) to reaction and involve nonadiabatic crossings to lower surfaces with lower barriers in all the explored regions $19000\text{--}25000 \text{ cm}^{-1}$.

In contrast with $5\text{A}'$, the $6\text{A}'$ PES and the surface above do not keep their asymptotic character in the Franck–Condon region as for the surfaces below. In particular, the $6\text{A}'$ PES is rather intriguing because it exhibits an avoided crossing that strongly depends on the Ca–F–C angle. The shape of the $5\text{A}'$ PES also depends markedly on the Ca–F–C angle. This region of the PES's has been explored in more detail than in our previous publications, using the calculation method outlined in section III. The corresponding results are shown in Figure 8.

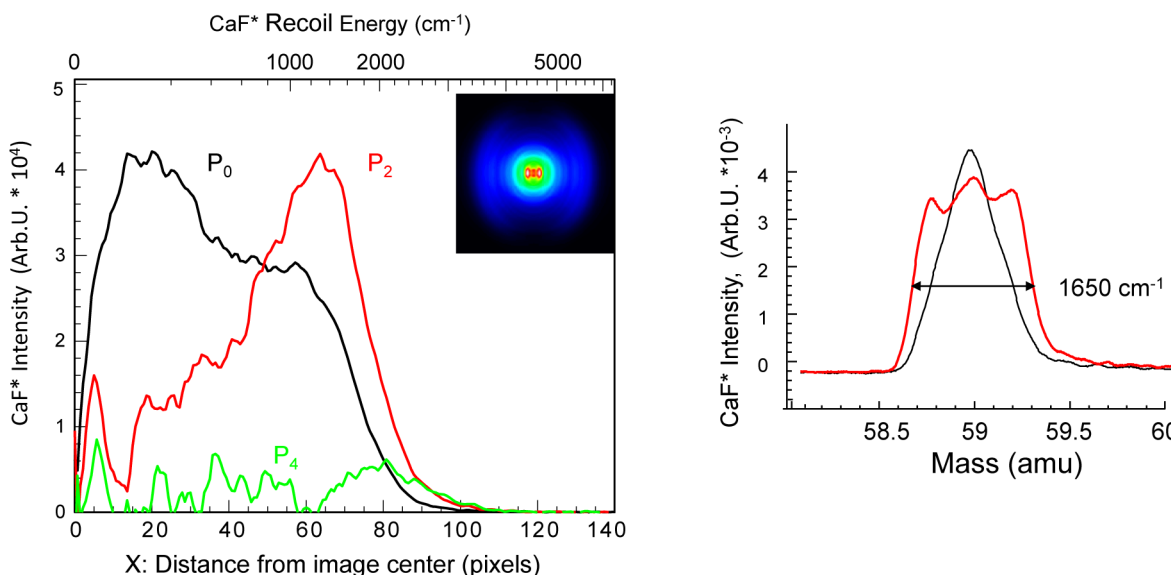


Figure 7. (Left) inverted image (pBasex) of the CaF velocity distribution excited at 370.1 nm. The P_2 , P_0 , and P_4 components of the Legendre expansion obtained from the image are presented in red, black, and green, respectively. (Right) profile of the CaF mass in the TOF, excitation 375 nm: red, parallel polarization to the molecular beam; black, perpendicular.

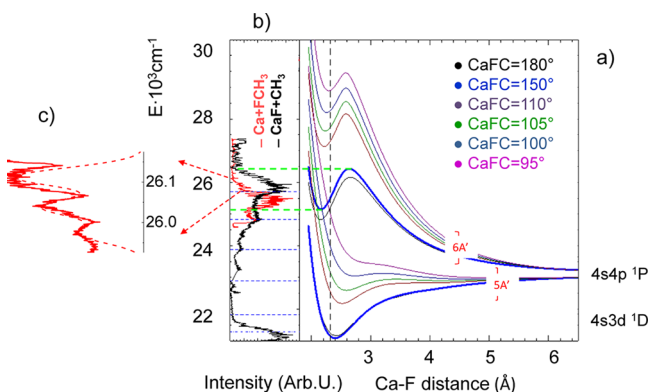


Figure 8. (a) Cuts of the $5A'$ and $6A'$ PES along the Ca–F coordinate for various Ca–F–C angles. (b) Action spectra: black, exploring channel 2, from ref 9; red exploring channel 1 by monitoring the $\text{Ca}(^1P_1)$ excited atom. The blue dashed bars indicate the vibrational progression in the C–F bond explicated in ref 9; the green dashed bars, the two extrema of suspended well resulting from the avoided crossing between the $6A'$ correlating with $\text{Ca}(4s4p)^1P_1$ and $7A'$ correlating with $\text{Ca}(4s5s)$. (c) Blow-up of the red action spectrum to channel 1 in (b).

The suspended well that appears along the $6A'$ cuts is due to an avoided crossing between the Σ -like repulsive surface correlating with $\text{Ca}(4s4p)^1P_1$ at large separation between Ca and CH_3F and a $7A'$ surface (not shown in the figure) correlating with the $\text{Ca}(4s5s)^1S_0$ state of strong Rydberg character. Due to this avoided crossing, the $6A'$ PES has a fairly strong charge transfer character in the Franck–Condon region. This was discussed in ref 10. We observe here that the height of the suspended well markedly depends on the Ca–F–C angle.

Action spectra are also shown in Figure 8. The black one exploring channel 2 is taken from ref 10 and the red one exploring channel 1 is from the present work, monitoring the $\text{Ca}(^1P_1)$ excited atom, while scanning the excitation laser in the 400–370 nm (25000 – 27000 cm^{-1}) region. As observed in the figure, excitation in this spectral region leads to the two output channels: the aforementioned channel 1 dissociation into Ca

$^1P_1 + \text{CH}_3\text{F}$ and the reactive channel channel 2, forming the excited CaF product + CH_3^* . The results presented in section IV.B and IV.C characterize the product recoil velocity distributions in the two channels. As discussed below, this allows unprecedented insight into the structure and excited state dynamics of the $\text{Ca}\cdots\text{FCH}_3^*$ complex.

V.A. $\text{Ca}\cdots\text{FCH}_3$ Complex, Ground State Energy Determination. The observed recoil energy variation of the calcium atom in the $\text{Ca}(4s4p)^1P_1$ state informs precisely on the energetics of ground state $\text{Ca}\cdots\text{FCH}_3$ complexes. The Ca^1P_1 fragment is identified at 40 amu and by a threshold for ionization at 390.3 nm ($25\,621\text{ cm}^{-1}$), compared to the known 389.8 nm ($25\,653\text{ cm}^{-1}$) value,²⁹ due to a $\sim 30\text{ cm}^{-1}$ Stark shift in the spectrometer.

The translational recoil energy of calcium increases linearly with excess energy as observed in Figure 5a. Therefore, the extrapolation to zero recoil energy; i.e., the threshold energy E_{ex} for the excited state dissociation of calcium yields an accurate measurement of the ground state energy of the complex E_{CaFCH_3} through the energy balance given in eq 6 below and represented in Figure 3 right:

$$E_{\text{ex}} = \text{KER} + E(\text{Ca}(^1P_1, 4s4p) \leftarrow (^1S_0, 4s^2)) + E_{\text{CaFCH}_3} \quad (6)$$

At $\text{KER} = 0$, one obtains $E_{\text{CaFCH}_3} = 24657 - 23652 = 1005\text{ cm}^{-1}$. This value is quite accurate, due to the linear extrapolation ($\pm 20\text{ cm}^{-1}$) and limited by the dispersion of the points. It yields a rather strong van der Waals bond owing to the very high polarizability of the calcium metal atom interacting with the dipole of CH_3F . It compares favorably with the calculated value, 850 cm^{-1} , obtained by quantum chemistry in ref 10.

V.B. Photodissociation Mechanism (Channel 1).

a. Mechanism Associated with Peak 1. The excited atom $\text{Ca}(^1P_1, 4s4p)$ atom recoils preferably aligned to the polarization of the laser which dissociates the $\text{Ca}\cdots\text{FCH}_3$ complex. The corresponding recoil energy varies linearly with the energy of the laser. The slope is 0.46 (Figure 4) in full agreement with an impulsive recoil between the calcium and fluorine in CH_3F .

The corresponding energy partitioning between Ca and CH₃F is indeed given by (mass of CH₃F)/(total mass) = 34/74 = 0.459 for Ca. Examining the peaked angular distribution of the recoiling Ca ¹P atom in Figure 4a, one finds the anisotropy of the recoil of the calcium atom indicates a prompt dissociation with $\beta_{2\text{diss}} = 1.7 \pm 0.15$, after correction by eq 5c. In particular, the dissociation is much prompter (see below, ~ 260 fs) than the rotation period of the excited complex ≈ 10 –30 ps and the observation of a Ca atom allows a characterization of the dissociation anisotropy. This fits also the observations in the TOF, which yield equivalent dissociation parameters.

We are left at this point with the conclusion that Ca ¹P recoils promptly along a molecular axis that is parallel to the transition moment of the excitation, i.e., parallel to the polarization direction of the excitation laser. The mechanism that is responsible for this is discussed now.

From the calculated potential energy curves shown in Figure 8, the only curves that correlate repulsively Ca ¹P(4s4p) at near collinear geometry (CaFC angle between 150 and 180°) is 6A', which is of Σ -like character and repulsive along the transition moment at large separation between Ca and CH₃F, beyond 2.7 Å. Following excitation toward this surface, the p ($\Omega = 0$) atomic orbital would be strongly repelled by methyl fluoride and Ca would obtain translational recoil parallel to the laser polarization. However, Figure 8 indicates also that the repulsive part of the curve 6A' is not accessible by Franck–Condon excitation from the ground state. The Ca–F equilibrium distance governing the Franck–Condon maximum from the ground state absorption is traced in dashed in Figure 8a. There is no intensity (10^{-5}) outside the suspended well in absorption from the ground state surface of the complex and this direct dissociation mode cannot yield the large abundance of Ca atoms observed experimentally.

Facing this conclusion, we need a dissociation mechanism with Ca atoms recoiling parallel to the dissociation laser but originating from the suspended well. A two-step scheme is presented involving a strong nonadiabatic coupling between the 6A' PES and 5A'.

As appears in Figure 8, the 6A' well is energetically degenerate with the 5A' PES correlating with (Ca¹P, $\Omega = 1$) + CH₃F, an in-plane Π -like potential, nonaccessible vertically by lack of Franck–Condon factors in this energy region. We infer that there is a strong non adiabatic coupling between the two 6A' and 5A' surfaces driven by the in plane Ca–F–C torsion. The wave function of the excited level extends from the Franck–Condon region to the inner part of the potential at small (Ca–F) distances where the nonadiabatic coupling V_{NA} should be at maximum. The coupling matrix element V_{NA} determines the dissociation rate k , along the Fermi Golden rule ($k = (2\pi/\hbar)\rho V_{\text{NA}}^2$) with ρ level density. As a nonadiabatic term, it depends not only on electronic terms of $\partial/\partial Q_i$ but also on the overlap (radial and angular) of the initial and final wave functions φ_i and φ_f through $V_{\text{NA}} = \langle \varphi_f | (\partial/\partial Q_i) | \varphi_i \rangle$. Examining Figure 8a, it appears that close to the inner limb of the suspended well, around the Ca–F–CH₃ angle of 150°, there is a region of angular and radial proximity between the 6A' (Σ -like) and 5A' (Π -like). The distance between cuts of the PES for a given angle is < 0.1 Å. The de Broglie wavelength characterizing the continuum wave function for the recoiling couple Ca, CH₃F with the 4500 cm⁻¹ excess energy to the bottom of the PES is ≈ 0.1 Å. One can then expect a good overlap at the equilibrium angle. The coupling should also be strong if one examines the cuts of the 6A' PES at various

angles; the $U(R_{\text{Ca-F}})_\theta$ potential is strongly dependent on the $\theta(\text{Ca-F-C})$ angle, resulting in an important $(\partial U/\partial \theta)$ value and a corresponding V_{NA} term through this term.³⁰

Hence, following the nonadiabatic transition, the system is placed on the repulsive Π , 5A' surface. The gradient along the Ca–F coordinate is much greater than the angular gradient and the complex with the available excess energy, dissociates very rapidly into Ca ¹P(4s4p) + FCH₃ in a *perpendicular fashion* (Π repulsive bond) to the Ca–F coordinate. As represented in Figure 9, the Ca–F dissociation coordinate is parallel to the

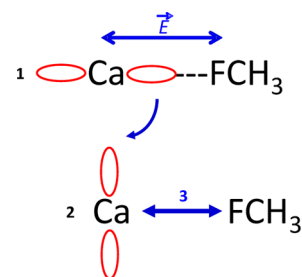


Figure 9. Indirect dissociation mechanism for channel 1. (1) Parallel, “ Σ ” type excitation by E . (2) Under the torque due to the Ca–F–C bending the Ca 4p orbital is flipped perpendicular in “ Π ” configuration. (3) Perpendicular, direct dissociation of the complex on the 5A' repulsive potential wall.

exciting laser polarization, as observed in the experiments. It seems we had observed a parallel dissociation. This stems from the rapid nonadiabatic transfer, much faster than the rotation of the complex. Indeed, looking at a blow-up of the action spectrum (red, panel c) for channel 1 in Figure 8b, resonances are seen, whose width can be simulated (c) with a 38 cm⁻¹ Gaussian function, corresponding to a ≈ 260 fs lifetime, as compared with the typical 10–30 ps rotational period of the complex. This is an $A' \rightarrow A'$ nonadiabatic transfer, but we note that even if there were some $A' \rightarrow A''$ nonadiabatic transfer, the resulting dissociation would occur along the Ca–F coordinate parallel to the laser polarization vector \vec{E} (for clarity the 3A'' surface is not reported in Figure 8, but qualitatively, it follows the 5A').

In conclusion, a complex mechanism has been unveiled where the dissociation to channel 1 seems direct but proceeds via a rapid nonadiabatic step that leads to a rapid overall dissociation consistent with the experimental observation with $\beta_{2\text{diss}} = 1.1 \pm 0.1$ to 1.7 ± 0.15 after use of eq 5c.

b. Peak 2 in Channel 1. A second maximum was found in the recoil distribution in Figure 4c. One can extrapolate in Figure 5a the energy dependence to zero recoil, obtaining 25 774 cm⁻¹. This places the dissociated system Ca + CH₃F, on a energy level higher by ≈ 1120 cm⁻¹, with respect to that of peak 1. A possibility is that a vibrationally excited mode of the CH₃F molecule is populated. In the free CH₃F molecule, there are indeed two modes, ν_1 (C–F stretch, 1048 cm⁻¹) and ν_6 (CH₃ rock, 1183 cm⁻¹),³¹ in the 1100 cm⁻¹ frequency range. Several observations are consistent with this assignment. First, in Figure 5a, the slope of the Ca atom recoil energy for this peak and the input energy is high, 0.42, close to that of peak 1, 0.46, and compares with the kinematic recoil limit 0.46, within experimental error. Second, as $\beta_2 \sim 1$ ($\beta_{2\text{diss}} \sim 1.1$), the dissociation proceeds faster than rotation because no randomization of the orientation of the calcium atom occurs. Third, the relative intensity of this peak (2) grows relative to peak (1)

with excitation energy, Figure 10. This dependence on the excess energy can be attributed to an increased overlap of the

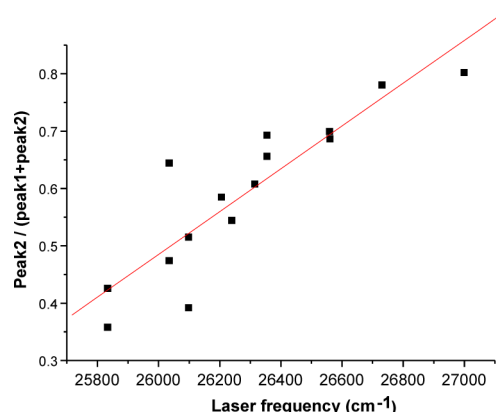


Figure 10. Fractional intensity of peak 2 in Figure 4 versus laser frequency, cm^{-1} .

wave functions with excess energy in the nonadiabatic process between the quasi-bound states in the suspended well of Figure 8a and the continuum wave functions of surface 5A'. The overlap is on the inner limb of the potential, where vibrational excitation in the suspended well brings the maximum of the vibrational wave function closer to the inner part of the potential.

Therefore, as soon as the dissociation to higher vibrational level becomes open, flux is observed in this channel, at least in the quasi linear geometries where the nonadiabatic transition 6A'–5A' occurs. It is likely that the C–F mode of CH_3F is the mode involved here, because the direction of the recoil will induce a compression of this mode. Then, among the degrees of freedom involved in the dissociation, the rotation of the CH_3F molecule should be excited through the Ca recoil. This does not appear in Figure 5 because the slopes of 0.46 close to the kinematic limit indicate no sharing of the recoil energy with another degree of freedom. This strongly suggests that the dissociation is extremely fast and does not let time to Ca to move around CH_3F and reach substantially bent geometries. Some rotational excitation may exist but to a small extent and smeared out within the 20 cm^{-1} precision of the present measurements.

c. Other Inelastic Channels. The lower $^1\text{D}(4s3d)$ state is also energetically accessible to the dissociation, but until the excitation-ionization laser is tuned below 365 nm (27400 cm^{-1}), it is not detectable by ionization. Actually, a very minor channel is detected below 365 nm (27400 cm^{-1}) in a 1/20 ratio as compared to the major channel 1. It is, however, difficult to extend this value to the whole range of the action spectrum because this wavelength is at its edge (Figure 8b).

For the same energetic reasons, the other channels leading to the $^3\text{P}(4s4p)$ and $^3\text{D}(3d4s)$ metastables are not considered because they are not ionized by the probe laser.

V.C. Branching the Flux between Dissociation and Reaction. From refs 9 and 10 we know that channel 2 leads to CaF through a prompt neutral reaction and we find here that it yields $\sim 6000\text{ cm}^{-1}$ KER in the products. This is in marked contrast with the excited state dynamics of $\text{Ba}\cdots\text{CH}_3\text{F}(\text{A}')$, where only direct dissociation into $\text{Ba} + \text{CH}_3\text{F}$ is observed and the BaF product arises from resonant two-photon ionization of the A' state into $(\text{Ba}\cdots\text{CH}_3\text{F})^+$, followed by reaction into

$\text{BaF}^+.$ ¹² Two points should be made here to show that the analysis of ref 12 does not apply here. First, the present weak and unfocused nanosecond laser excites a very short-lived intermediate of the complex. It is unable to ionize the excited complex during its short lifetime, as it was the case for $\text{Ba}\cdots\text{CH}_3\text{F}$ with a powerful femtosecond laser of comparable time duration with the decaying excited state. Second, here, the KER assigned to CaF in the present experiment at 26000 cm^{-1} (385 nm) is high and consistent with dynamics along a repulsive reaction surface where much energy is disposed into translational recoil. In contrast, if CaF were formed as a CaF^+ ion, it would have to overcome the very attractive $\text{F}\cdots\text{Ca}\cdots\text{CH}_3^+$ well³² and energy would be disposed in the internal modes. Small KER would be expected in contradiction with the present experimental results. Hence we conclude that the reaction to CaF^* proceeds actually in the neutral excited state of $(\text{Ca}\cdots\text{FCH}_3)^*$ prior to ionization.

As for the calcium atom recoil, the CaF product shows an important apparent recoil anisotropy in Figure 7, $\beta_2 = 1.6 \pm 0.15$, though we cannot correct for the angle dependency of the ionization probability of CaF. This β_2 indicates a rapid evolution toward CaF, such that the complex has not substantially reoriented after the excitation, i.e., in 10–30 ps. The recoil fraction is 0.23 from the slope in Figure 5b, equal to the kinematic limit $15/74$. The linearly extrapolated value for laser excitation at 21419 cm^{-1} yields the final state without kinetic energy (aside from electronic). Because the slope of the dependence of the recoil with laser energy in Figure 5b is equal to the kinematic limit, no variation is expected for the internal energy with the exciting laser. The internal energy must stay constant through the range explored here ($\sim 3000\text{ cm}^{-1}$). The extrapolated value corresponds to a level (or group of levels) at 27420 cm^{-1} , when referenced to CaF (X), ground state (Figure 3). The closest energetically accessible electronic energy levels of CaF are the $\text{B}(^2\Sigma)$ or $\text{B}'(^2\Delta)$ states respectively at ~ 18800 or 21574 cm^{-1} ,³³ but the C state is too high at 30255 cm^{-1} . Thus, $\sim 6000\text{ cm}^{-1}$ internal energy is deposited on the CaF B' excited state and CH_3 . This high vibrational excitation fits with the harpoon model for the reaction at the transition state. Also in favor of the CaF B' detection, the ionization thresholds of 28194 cm^{-1} (355 nm) for the B state or 25420 cm^{-1} (393.4 nm) for the B' state (vibrationless), with the ionization potential of CaF 5.8270 eV (46994 cm^{-1}).³⁴ With the ionization laser in the 26000 cm^{-1} (385 nm) range, the B' state will be preferentially ionized with a $\sim 6000\text{ cm}^{-1}$ vibrational energy. This definitely points to a rapid reaction process.

We observed that the $\text{Ca } ^1\text{D}_2(4s3d)$ showed only a minor population through a nonadiabatic process following the absorption in the 6A' suspended well. The reason could be that, instead of forming Ca^* , this channel leads to reaction forming CaF^* . Indeed, examining Figure 8 in ref 9 we find that a barrierless path leading from Ca^1D ("Π or Δ" surfaces) to CaF B'. Using the same arguments as for channel 1, the nonadiabatic relaxation to Ca^1D creates a "Π, Δ" oriented atom, hence a recoiling CaF ($^2\Delta$) along the Ca–F axis, and CaF^* shows an apparent parallel recoil to the laser polarization in agreement with this scheme.

VI. CONCLUSION

We have investigated by a combined experimental and quantum chemical approach, a rather seldom situation in reaction dynamics: the effective competition between reaction

and inelastic scattering, because usually the latter process, occurring at longer intermolecular distances is dominant over a reaction that necessitates a closer approach. Here, this occurrence rests on the specificity of the potential energy surface calculated in the energy range investigated (25000–28000 cm⁻¹). A quasi-bound well traps the system and allows a partition of the outgoing fluxes. The system, the electronically excited Ca⁺·FCH₃ complex undergoes a rapid predissociation to two distinct surfaces leading to inelastic scattering and reactive scattering. The absorption is to the 6A' suspended well resulting from an avoided crossing between an attractive Rydberg surface correlating with Ca(4s5s)¹S₀ + CH₃F and a repulsive surface correlating with Ca(4s4p)¹P₁ + CH₃F. This forms Ca ¹P (inelastic scattering) and CaF B' (reactive scattering), in variable but comparable amounts with excitation energy.

Though action spectra detecting either channel inform precisely on the initial and transition states, here the suspended well, the observation of the KER, and the polarization recoil have allowed deciphering the post-transition state evolution. In the inelastic channel, the dissociation is quasi direct and the KER is within the kinematic recoil limit; moreover, it occurs parallel to the incident laser polarization. This has been interpreted as a scheme with a rapidly evolving 6A' intermediate:

6A' absorption ("Σ symmetry")

→ nonadiabatic transfer to 5A' (Π)

→ Π oriented rapid dissociation

The same scheme also applies for the reaction forming CaF, where the separation from the other channel appears through a nonadiabatic coupling from the intermediate 6A' to a different competing channel, Ca¹D. The separation between the two fluxes derives from the branching ratios in the nonadiabatic relaxation. In addition, recording the anisotropy and KER simultaneously for both channels by TOF measurements allows a simple and direct comparison of their relative intensities, which are equal for 380 nm excitation.

The investigation of the kinetic energy release in the dissociation of reacting complexes is, with the measurement of the alignment in the recoil of the fragments a powerful tool for explaining post-transition state evolution and extremely powerful when a single atom is ejected. It would be also highly desirable to be able to perform photoelectron spectra on selected fragments, either the excited Ca atom or the reaction product CaF. This necessitates an experiment where the electrons would be detected in coincidence with specified ions. This cannot be done with the present lasers operating with a 10 Hz repetition rate. Nevertheless, this must be a strong motivation for future experiments, which would fully specify the symmetry of the final states that are probed. Hence, such experiments would provide almost direct information on the nonadiabatic transition process, which is at the center of the present dynamics.

■ APPENDIX 1: DETERMINATION OF THE ANGLE DEPENDENT IONIZATION PROBABILITY OF THE EXCITED CALCIUM ATOM

The calcium atom recoils from CH₃F with an angle θ from the polarization vector **E** in the lab frame. We shall project the molecular frame vectors in the laboratory frame. After

dissociation ($R \rightarrow \infty$), the calcium atom is produced with angular momentum j and projection Ω on the intermolecular axis R (Figure 1b): eigenstates $|j\Omega\rangle$. In terms of the eigenstates, $|jm\rangle$ (m being the projection of j on the laboratory axes defined in this case by the laser polarization, the $|j\Omega\rangle$ are decomposed as

$$|j\Omega\rangle = \sum_m D_{m\Omega}^j(\Phi, \Theta, 0) |jm\rangle$$

If photoionization proceeds via a transition $j \rightarrow j'$, the total photodissociation cross section will be given by

$$I(\theta) = W(\theta) \times (1 + \beta_{2\text{diss}} P_2(\theta)) \quad \text{where}$$

$$W(\theta) \propto \sum_{m'} | \langle j\Omega | Y_{10} | j'm' \rangle |^2$$

Because

$$\langle j\Omega | Y_{10} | j'm' \rangle \propto \sum_m D_{m\Omega}^j(\Phi, \Theta, 0) \begin{pmatrix} j & 1 & j' \\ m & 0 & m' \end{pmatrix}$$

we get

$$W(\theta) \propto \sum_m |D_{m\Omega}^j(\Phi, \Theta, 0)|^2 \begin{pmatrix} j & 1 & j' \\ m & 0 & -m \end{pmatrix}^2$$

Here $j = 1$ and $j' = 2$ (d electron wave)

$$\begin{aligned} W(\theta) &\propto \sum_m |D_{m\Omega}^1(\Phi, \Theta, 0)|^2 (4 - m^2) \\ &= 4 |D_{0\Omega}^1|^2 + 3(|D_{1\Omega}^1|^2 + |D_{-1\Omega}^1|^2) \end{aligned}$$

When $\Omega = 0$,

$$\begin{aligned} |D_{00}^1|^2 &= (\cos \theta)^2, \\ |D_{-10}^1|^2 &= |D_{10}^1|^2 = \frac{1}{2} (\sin \theta)^2 \end{aligned}$$

and

$$W(\theta) \propto 1 + \frac{1}{3} (\cos \theta)^2$$

When $\Omega = \pm 1$,

$$\begin{aligned} |D_{0\pm 1}^1|^2 &= \frac{1}{2} (\sin \theta)^2, \\ |D_{1\pm 1}^1|^2 &= \frac{1}{4} (1 \pm \cos \theta)^2, \\ |D_{-1\pm 1}^1|^2 &= \frac{1}{4} (1 \mp \cos \theta)^2 \end{aligned}$$

and

$$W(\theta) \propto 1 - \frac{1}{7} (\cos \theta)^2$$

If $|\Omega| = 1$

$$\begin{aligned} I(\theta) &= W(\theta) \cdot (1 + \beta_{2\text{diss}} P_2(\theta)) \\ &= \left(1 - \frac{1}{7} (\cos \theta)^2\right) \cdot (1 + \beta_{2\text{diss}} P_2(\theta)) \end{aligned}$$

$$I(\theta) \propto \left(70 - \frac{7}{5}\beta_{2\text{diss}}\right) + (68\beta_{2\text{diss}} - 7) \cdot P_2(\theta) - \frac{18}{5}\beta_{2\text{diss}} \cdot P_4(\theta) \quad (\text{Sb}')$$

and the apparent alignment

$$\beta_2 = \frac{68\beta_{2\text{diss}} - 7}{70 - \frac{7}{5}\beta_{2\text{diss}}} \quad (\text{Sc}')$$

Also for $\Omega = 0$,

$$I(\theta) = (50 + 2\beta_{2\text{diss}})/45 + P_2(\theta)(2/9 + 74\beta_{2\text{diss}}/63) + 4\beta_{2\text{diss}} \cdot P_4(\theta)/35$$

The apparent alignment is

$$\beta_2 = (2/9 + 74\beta_{2\text{diss}}/63)/((50 + 2\beta_{2\text{diss}})/45)$$

for $\Omega = 0$.

■ ASSOCIATED CONTENT

■ Supporting Information

S1: Simulation of the mass profiles due to the recoiling fragments. S2: Stark effect on the ionization potential. This material is available free of charge via the Internet at <http://pubs.acs.org>.

■ AUTHOR INFORMATION

Corresponding Author

*B. Soep. E-mail: benoit.soeep@cea.fr.

Notes

The authors declare no competing financial interest.

■ ACKNOWLEDGMENTS

L.P. acknowledges the support of contract ANR-09-JCJC-0090-01 CHROMADYNE. We also thank André Szwec of the ISMO laboratory at Université Paris Sud, for his contribution to the mechanical construction of the VMI. S.S. and B.S. acknowledge the "Triangle de la Physique" (contracts STOLTE and NOSTADYNE no2010-004-T) for funding and the Marie Curie network EU-ITN project ICONIC-238671.

■ REFERENCES

- (1) Breckenridge, W. H.; Juvet, C.; Soep, B. Orbitally selective chemical reaction in Hg-H₂ van der Waals complexes. *J. Chem. Phys.* **1986**, *84*, 1443–1450.
- (2) Juvet, C.; Boivineau, M.; Duval, M. C.; Soep, B. Photochemistry in excited states of van der Waals complexes. *J. Phys. Chem.* **1987**, *91*, 5416–5422.
- (3) Topaler, M. S.; Truhlar, D. G.; Xiao Yan, C.; Piecuch, P.; Polanyi, J. C. The photoabsorption spectrum of Na···FH van der Waals molecule: comparison of theory and experiment for a harpooning reaction studied by transition state spectroscopy. *J. Chem. Phys.* **1998**, *108*, 5378–5390.
- (4) Wittig, C.; Sharpe, S.; Beaudet, R. A. Photoinitiated reactions in weakly bonded complexes. *Acc. Chem. Res.* **1988**, *21*, 341–347.
- (5) Manolopoulos, D. E.; Stark, K.; Werner, H.-J.; Arnold, D. W.; Bradforth, S. E.; Neumark, D. M. The transition state of the F + H₂ reaction. *Science* **1993**, *262*, 1852–1855.
- (6) Briant, M.; Fournier, P. R.; Gaveau, M. A.; Mestdag, J. M.; Soep, B.; Visticot, J. P. Excited state reactions of metals on clusters: full dynamics of the Ca* + HBr reaction on Ar-2000. *J. Chem. Phys.* **2002**, *117*, 5036–5047.

(7) Scherer, N. F.; Khundkar, L. R.; Bernstein, R. B.; Zewail, A. H. Real-time picosecond clocking of the collision complex in a bimolecular reaction: the birth of OH from H+CO₂. *J. Chem. Phys.* **1987**, *87*, 1451–1453.

(8) Soep, B.; Abbes, S.; Keller, A.; Visticot, J. P. State selective reactions prepared through the excitation of orbital states in calcium-hydrogen halide van der Waals complexes (Ca-HX*). *J. Chem. Phys.* **1992**, *96*, 440–449.

(9) Gloaguen, E.; Sanz-Sanz, C.; Collier, M.; Gaveau, M. A.; Soep, B.; Roncero, O.; Mestdag, J. M. Transition-state spectroscopy of the photoinduced Ca+CH₃F reaction. 3. Reaction following the local excitation to Ca(4s3d ¹D₁). *J. Phys. Chem. A* **2008**, *112*, 1408–1420.

(10) Mestdag, J. M.; Spiegelman, F.; Gloaguen, E.; Collier, M.; Lepetit, F.; Gaveau, M. A.; Sanz, C.; Soep, B. Transition state spectroscopy of the photoinduced Ca+CH₃F reaction. 2. Experimental and ab initio studies of the free Ca···FCH₃ complex. *J. Phys. Chem. A* **2006**, *110*, 7355–7363.

(11) Gaveau, M. A.; Gloaguen, E.; Fournier, P. R.; Mestdag, J. M. Transition state spectroscopy of the photoinduced Ca + CH₃F reaction. 1. A Cluster Isolated Chemical Reaction Study. *J. Phys. Chem. A* **2005**, *109*, 9494–9498.

(12) Stert, V.; Ritze, H. H.; Radloff, W.; Gasmi, K.; Gonzalez-Urena, A. Wave packet dynamics on the repulsive potential surface of Ba···FCH₃ excited at 745 nm. *Chem. Phys. Lett.* **2002**, *355*, 449–456.

(13) Eppink, A. T. J. B.; Parker, D. H. Velocity map imaging of ions and electrons using electrostatic lenses: application in photoelectron and photofragment ion imaging of molecular oxygen. *Rev. Sci. Instrum.* **1997**, *68*, 3477–3484.

(14) Proch, D.; Trickl, T. A high-intensity multi-purpose piezo-electric pulsed molecular-beam source. *Rev. Sci. Instrum.* **1989**, *60*, 713–716.

(15) Wiley, W. C.; McLaren, I. H. Time-of-flight mass spectrometer with improved resolution. *Rev. Sci. Instrum.* **1955**, *26*, 1150–1157.

(16) Simons, J. P. Dynamical stereochemistry and the polarization of reaction products. *J. Phys. Chem.* **1987**, *91*, 5378–5387.

(17) Mons, M.; Dimicoli, I. Photodissociation of NO₂. Internal energy distribution and anisotropies in the fragments. *Chem. Phys.* **1989**, *130*, 307–324.

(18) Garcia, G. A.; Nahon, L.; Powis, I. Two-dimensional charged particle image inversion using a polar basis function expansion. *Rev. Sci. Instrum.* **2004**, *75*, 4989–4996.

(19) Spiegelman, F.; Maron, L.; Breckenridge, W. H.; Mestdag, J. M.; Visticot, J. P. Two-electron pseudopotential investigation of the electronic structure of the CaAr molecule. *J. Chem. Phys.* **2002**, *117*, 7534–7550.

(20) Werner, H.-J.; Knowles, P.; Lindh, R.; Manby, F.; Schütz, M.; Celani, P.; Korona, T.; Rauhut, G.; Amos, R.; Bernhardsson, A. MOLPRO, version 2006.1, a package of ab initio programs. See <http://www.molpro.net>, 2006.

(21) Kendall, R. A.; Dunning, T. H.; Harrison, R. J. Electron-Affinities of the 1st-Row Atoms Revisited - Systematic Basis-Sets and Wave-Functions. *J. Chem. Phys.* **1992**, *96*, 6796–6806.

(22) Werner, H. J.; Knowles, P. J. An efficient internally contracted multiconfiguration-reference configuration interaction method. *J. Chem. Phys.* **1988**, *89*, 5803–5814.

(23) Knowles, P. J.; Werner, H. J. An efficient method for the evaluation of coupling coefficients in configuration interaction calculations. *Chem. Phys. Lett.* **1988**, *145*, 514–522.

(24) Knowles, P. J.; Werner, H. J. An efficient second-order MC SCF method for long configuration expansions. *Chem. Phys. Lett.* **1985**, *115*, 259–267.

(25) Werner, H. J.; Knowles, P. J. A second order multiconfiguration SCF procedure with optimum convergence. *J. Chem. Phys.* **1985**, *82*, 5053–5063.

(26) Sugar, J.; Corliss, C. Atomic energy levels of the iron period elements potassium through nickel. *J. Phys. Chem. Ref. Data* **1985**, *14*, 1–664.

- (27) Karny, Z.; Zare, R. N. Effect of vibrational excitation on molecular beam reactions of Ca and Sr with HF and DF. *J. Chem. Phys.* **1978**, *68*, 3360–3365.
- (28) Weast, R. C.; Astle, M. J.; Beyer, W. H. *CRC Handbook of Chemistry and Physics*; CRC: Boca Raton, FL, 1984.
- (29) <http://physics.nist.gov/PhysRefData/Handbook/Tables/calciumtable5.htm>. In *Handbook of Basic Atomic Spectroscopic Data*; NIST: Gaithersburg, MD.
- (30) Englman, R.; Jortner, J. The energy gap law for radiationless transitions in large molecules. *Mol. Phys.* **1970**, *18*, 145–164.
- (31) Nikitin, A. V.; Rey, M.; Tyuterev, V. G. Rotational and vibrational energy levels of methyl fluoride calculated from a new potential energy surface. *J. Mol. Spectrosc.* **2012**, *274*, 28–34.
- (32) Harvey, J. N.; Schroder, D.; Koch, W.; Danovich, D.; Shaik, S.; Schwarz, H. Electron-transfer reactivity in the activation of organic fluorides by bare metal monocations. *Chem. Phys. Lett.* **1997**, *273*, 164–170.
- (33) Verges, J.; Effantin, C.; Bernard, A.; Topouzkhanian, A.; Allouche, A. R.; d’Incan, J.; Barrow, R. F. The B' $^2\Delta$ state of CaF. *J. Phys. B: At., Mol. Opt. Phys.* **1993**, *26*, 279.
- (34) Jakubek, Z. J.; Harris, N. A.; Field, R. W.; Gardner, J. A.; Murad, E. Ionization potentials of CaF and BaF. *J. Chem. Phys.* **1994**, *100*, 622–627.